Journal of Colloid and Interface Science 632 (2023) 326–334

Contents lists available at ScienceDirect

Journal of Colloid and Interface Science

journal homepage: www.elsevier.com/locate/jcis

Highly promoted solvent-*co*-intercalation process in pencil graphite anode and $Na_3V_2(PO_4)_3$ cathode in full-cell Na-ion battery

Krishnan Subramanyan [a], Yun-Sung Lee [b,*], Vanchiappan Aravindan [a,*]

[a] Department of Chemistry, Indian Institute of Science Education and Research (IISER), Tirupati 517507, India
[b] School of Chemical Engineering, Chonnam National University, Gwang-ju 61186, Republic of Korea

GRAPHICAL ABSTRACT

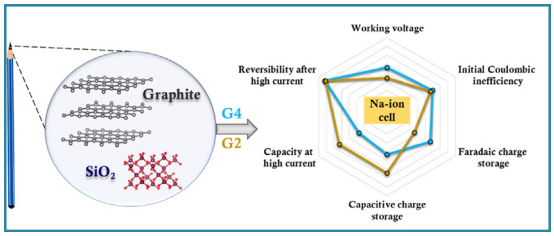

ARTICLE INFO

Article history:
Received 22 October 2022
Revised 9 November 2022
Accepted 11 November 2022
Available online 19 November 2022

Keywords:
Na-ion battery
Anode
Graphite
Ethers
Solvent-*co*-intercalation

ABSTRACT

The electrochemical performance of graphite recovered from 6H-pencil with the highest content of SiO_2 is evaluated in both Na-ion half and full-cell assemblies. The concept of sodium co-intercalation into graphite is exploited by fabricating cells with electrolytes based on tetraethylene glycol dimethyl ether (G4) and diethylene glycol dimethyl ether (G2). The capacity at high current rates is maximum when the G2-based electrolyte is used, both in half and full cells, while the capacity retention after high current rates is better in a G4-based system. Upon calculating the capacity contribution, the G2-based system shows prominent capacitance-based charge storage, whereas the G4-based system has a higher contribution from the Faradaic mechanism. The former also shows a faster diffusion mechanism. While G2 based system has higher capacity retention in half-cell, G4 based system has higher capacity retention in full-cell. When G2 is used as the electrolyte solvent, the irreversibility during cycling is high, affecting cell performance. The full cells with G4 and G2 electrolytes show maximum energy/power densities of 33 Wh kg^{-1}/2.7 kW kg^{-1} and 23 Wh kg^{-1}/1.4 kW kg^{-1}, respectively. Our study shows that the charge storage mechanism can be varied by tuning the electrolyte solvent. This study is the first to explore pencil graphite for sodium-ion storage.

1. Introduction

Electrochemical energy storage devices are effective tools for avoiding the intermittent and discontinuous nature of renewable energy sources and enabling easy load levelling. Lithium-ion batteries (LIBs) are a paradigm shift in electrochemical energy storage devices with a higher specific capacity, operating voltage, no memory effect, and require less maintenance than their predecessors. Graphite as an anode has been explored for LIBs due to its high specific capacity, low lithiation/de-lithiation potential, small voltage hysteresis, and robust cycling ability[1–3]. Research is now focused on post-LIB technologies for better energy and power density, higher operating potential, lower cost, and improved safety [4,5]. Among these, the sodium-ion battery is a promising candi-

* Corresponding authors.
E-mail addresses: leeys@chonnam.ac.kr (Y.-S. Lee), aravind_van@yahoo.com (V. Aravindan).

https://doi.org/10.1016/j.jcis.2022.11.053
0021-9797/

date because of the abundance of sodium, the ability to use aluminium as an anode current collector, the geographical uniformity of sodium distribution, and so on[6,7]. Although lithium and sodium are elements of the same group in the periodic table, a smooth transition from lithium to sodium was not possible. One reason is that graphite half-cells with ester-based electrolytes displayed very low sodium storage abilities due to the instability of the binary graphite intercalation compound with Na (*b*-GIC)[8]. Furthermore, the bulkiness of sodium introduces a higher structural deformation energy[9]. Nevertheless, using ether-based solvents as electrolytes, ultra-stable sodium-ion storage could be set up in graphite, with a lower specific capacity than lithium[10,11]. This is accomplished by forming a ternary-GIC (*t*-GIC) which prevents the decomposition of [Na-*co*-solvent]$^+$ as its LUMO energy levels are above the graphite Fermi levels[12–14].

The most accessible source of graphite in our everyday life is pencil lead[15]. Pencils are coded based on hardness (H) and blackness (B), with numbers prefixing the symbol to signify the degree of hardness or blackness. The pencils we purchased ranged from 12B to HB to 6H. A pencil with the initials HB stands for hard-black (medium hardness and blackness). The constituents of pencil lead, graphite, and clay (SiO_2) determine the darkness and hardness, respectively. The glue that binds the components together is another component of the pencil lead. The clay content increases as the code progress from HB to 6H, increasing the hardness of the lead. The graphite content determines the pencil's darkness, which is greatest in 12B. Pencil graphite was previously investigated for energy storage applications, particularly supercapacitors. Zheng *et al.*[16] fabricated a stable supercapacitor with cellulose paper electrodes where graphite is deposited from pencil lead by drawing on the paper. This solvent-free approach resulted in a multi-layered graphene structure that could impart high areal capacitance and long-term cycling stability. Yao *et al.* [17] fabricated a flexible solid-state supercapacitor, where a graphite/polyaniline electrode was prepared by drawing with pencil on paper, followed by electrodeposition and assessed the influence of the polyaniline nanowire network on the capacitance. Chen *et al.* [18] reported the exfoliation of pencil graphite into graphene with the help of nanoclay, which can be subsequently used as electrodes for energy storage or as a current collector. Aside from these, the properties of pencil graphite have been studied and used as electrodes in various applications [19–23]. Trnkova *et al.* [24] modified pencil graphite through chemical and thermal treatments and studied the morphology changes and the variation in electrochemical performance.

The lithium and potassium storage in the pencil-trace anode was explored by Tai *et al.* [25], where pencil traces were made on the separator filter paper. Subsequently, these were used as a current collector-free anode for lithium and potassium-ion half-cells with conventional ester-based electrolytes. Such a mode of fabrication can provide low active mass loading of 0.5–1.0 mg cm^{-1}. By powdering pencil lead and coating it on copper foil, Mamidi *et al.* [26] fabricated pencil graphite electrodes with a mass loading of 2.2 mg cm^{-1}. Our group has explored the Li-ion storage ability of pencil graphite in a Li-ion capacitor and in a binder-free Li-ion micro-capacitor, which provided promising results [27,28]. In this work, we coupled the glyme-assisted sodium storage with the graphitic nature of pencil with the highest SiO_2 content *via* the solvent-*co*-intercalation process. We evaluated the performance of 6H graphite using tetraethylene glycol dimethyl ether (TEGDME, G4) and diethylene glycol dimethyl ether (DEGDME, G2). In both electrolyte systems, the cycling performance of 6H graphite was stable. Among the electrolytes tested, the G4-based system demonstrated lower irreversibility and improved performance in full-cell configuration. The cyclic voltammetry (CV) curves differed in peaks and peak positions for different electrolyte compositions. Despite outperforming the G4-based system in half-cell mode, the G2-based system struggled in full-cell mode due to high irreversibility. G2-based and G4-based half-cells displayed an initial charge capacity of 140 mAh g^{-1} at 0.05 A g^{-1} with a charge capacity retention of 99 and 93% after 200 cycles. It was discovered that the G2-based system stores Na-ion primarily through a capacitive charge storage mechanism, whereas the G4-based system stores Na-ion primarily through the Faradaic mechanism. The novel aspect of Na-ion storage in pencil graphite is investigated in this work, and the performance with various electrolyte solvents is compared. This work aims to investigate a capacitive-*co*-intercalation coupled mechanism for increasing the power density of a co-intercalation-based full-cell.

2. Experimental section

***Recovery of 6H*:** Pencils were purchased from Kasimir drawing pencils. The graphite from the 6H pencil was recovered directly without any further purification. The pencil lead from the 6H pencil was removed, and any wooden pieces from the pencil were carefully eliminated. Afterwards, this was subjected to high-energy mechanical milling (HEMM) in Spex SamplePrep 8000D Mixer/Mill for five minutes. The procedure is summarized in Scheme 1. The work aims to investigate a capacitive-*co*-intercalation coupled mechanism for increasing the power density of a co-intercalation-based full-cell.

***Synthesis of carbon-coated $Na_3V_2(PO_4)_3$ (NVPC)*:** NVPC synthesis has been performed *via* a ball milling–pyrolysis route mentioned in a previous report [29]. Initially, $NaH_2PO_4{\cdot}H_2O$ (Extra Pure, HIMEDIA), NH_4VO_3 (>99%, Sigma Aldrich), and citric acid (>99.5%, Sigma Aldrich) were mixed in a 3:2:3 M ratio. Ethanol was added to the above mixture and then subjected to planetary ball milling in Retsch PM 200 for 24 h at 300 rpm. The ball-to-material mass ratio is maintained at 6:1. After ball milling, the obtained mixture was kept in a 70 °C oven overnight to dry completely. The dried mixture was ground in an agate mortar pestle, followed by pyrolysis at 800 °C for 8 h. A 5 °C min^{-1} heating ramp rate was used and subsequently naturally cooled to room temperature.

Material characterization: Using monochromatic Cu K α radiation of wavelength λ = 1.5604 Å in Rigaku Smartlab automated multipurpose X-ray diffractometer, the crystal structure of 6H-graphite and NVPC was conducted at a scan rate of 0.5° min^{-1}. Raman spectroscopy of 6H pencil graphite was performed in Lab-Ram HR800 UV Raman microscope (Horiba Jobin– Yvon, France) with a 515 nm diode laser as a light source at room temperature. The materials' surface composition was evaluated through X-ray photoelectron spectroscopy (XPS, Multilab, 2000, UK). Imaging techniques, include field emission scanning electron microscopy (FE-SEM S-4700, Hitachi, Japan) and high-resolution transmission electron microscopy (HR-TEM, JEM-2000, EX-II, JEOL, Japan) were carried out to study the surface and internal structure of the materials, respectively. Estimation of the carbon content in 6H-graphite and NVPC is done in thermogravimetric analysis (TGA, Shimadzu, Japan), with a ramp rate of 5 °C min^{-1} in the air atmosphere.

2.1. Electrochemical characterization

***6H and NVPC electrodes*:** The graphite obtained from the 6H pencil was coated on copper foil. Initially, polyvinylidene fluoride binder (PVDF) is dissolved in 1–Methyl–2–pyrrolidinone (NMP, anhydrous, Sigma Aldrich, >99.5%). The conductive additive (acetylene black, AB) and active material (6H-graphite) were added. PVDF, AB and 6H-graphite were added in 80:10:10 (wt.%) ratio. A homogenous slurry was prepared by stirring the above mixture

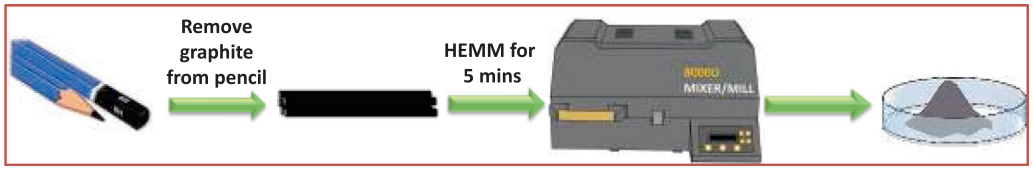

Scheme 1. Recovery of graphite from 6H pencil.

overnight at room temperature. The slurry was cast onto Cu-foil using the doctor blade technique and completely dried at 65 °C in an air oven. The coated electrode was pressed in a calendar roller machine and punched into 12 mm electrodes. The obtained electrodes were stored in a dry cabinet and assembled in half and full–cells. To fabricate NVPC electrodes, an NVPC-AB-teflonized acetylene black (TAB, binder) free-standing film was pressed onto a 14 mm stainless steel mesh (Goodfellow, UK) in a pellet maker using Specac hydraulic press. While making the film, ethanol was used as a solvent to make the binder flexible. The constituents were used in a ratio of 4:2:1 (wt.%). NVPC electrodes for full-cells were fabricated with the same ratio after balancing the mass according to the capacity of the anode measured during pre-cycling.

Half and full-cell studies: 6H-graphite and NVPC were assembled into half-cells with sodium metal foil as reference and counter electrode. Cell fabrication is performed in an MBraun inert glove box workstation with O_2 and H_2O levels below 0.1 ppm. Half and full-cells have been fabricated in a CR2016 coin cell with a glass microfiber separator (Whatmann, cat no. 1825–047, UK). 6H-graphite electrodes were dried for 4 h in a 75 °C vacuum oven, whereas the NVPC electrode was dried for at least 24 h. Two electrolytes were developed with sodium trifluoromethanesulfonate ($NaCF_3SO_3$, 98%, Sigma Aldrich) as the salt. One made use of tetraethylene glycol dimethyl ether (G4, TEGDME, >99%, Sigma Aldrich), whereas the other used diethylene glycol dimethyl ether (G2, DEGDME, anhydrous, >99.5%, Sigma Aldrich) as a solvent. After preparing the electrolytes, molecular sieves were added and kept for 24 h before using them to remove any excess moisture. 6H was pre-cycled five times before full-cell fabrication to mitigate the initial irreversibility in its capacity. The electrode was then carefully removed from the half-cell and assembled in a full-cell with an NVPC cathode whose mass is calculated based on the capacity and mass of the pre-cycled half-cell active material. The specific capacity of 6H-graphite is calculated by taking 46.16% of the mass of 6H-graphite in TGA, and it was seen that 6H-graphite contains 53.84% of SiO_2, which doesn't contribute to Na-ion storage. All electrochemical tests were performed in a BioLogic battery tester (BCS-805).

3. Results and discussion

The crystal structure of the 6H pencil graphite is examined using X-ray diffraction (XRD), whose pattern is given in Fig. 1a. The sharp peaks reveal the highly crystalline nature of pencil graphite, demonstrating that high-energy ball milling does not destroy the ordered structure of pencil graphite. The peaks at 2 θ values of 26.5° and 54.7° match DB card #00–056-0160 with space group 194: *P*63/*mmc*, corresponding to (002) and (004) planes, which belong to the 2H-graphite. 2H denotes hexagonal and ABAB carbon layering, with the B layer shifting slightly relative to the A layer. In addition, multiple peaks with a lower intensity correspond to SiO_2 (DB card # 00–001-0649) with space group 154: *P*3221. The source of SiO_2 is clay, which is added to the pencil to increase its hardness. SiO_2 content is anticipated to be high in 6H due to its increased thickness.

Raman spectra (Fig. 1b) consist of a sharp peak at 1579 cm^{-1}, a small broad peak at 2670 cm^{-1}, and a smaller broad peak at 1352 cm^{-1}. These correspond to carbonaceous material's characteristic G, 2D, and D bands. The I_D/I_G ratio is 0.2, confirming a highly ordered structure visible in the XRD analysis. The 2D peak profile agrees with a highly ordered multi-layer graphitic structure [30].

The carbon content in 6H pencil lead is estimated in thermogravimetric analysis (TGA). TGA was performed from room temperature to 900 °C at 10 °C $min.^{-1}$ (Fig. 1c). There was no significant weight loss till 600 °C (~3 wt.%). Beyond this temperature, there was a sharp decrease in sample weight, resulting in a total weight loss of approximately 46.16 wt.%. This weight loss indicates the oxidation of graphite, and the weight loss signifies the amount of graphite present in the sample [31]. All the capacity calculations for the half and full-cells have been performed with the mass of graphite alone since SiO_2 is electrochemically inactive for Na-ion storage. The elemental constitution was further confirmed by performing an X-ray photoelectron spectroscopy (XPS). The XPS survey spectrum (**Fig S1**) shows the presence of C, O, and Si. The carbon XPS peak can be deconvoluted into three peaks (Fig. 1d) centred at 284.6, 286.1, and 289.5 eV that belong to C—C sp^2 bond C—O, and C—C/C–H, respectively [32,33]. The O1s peak can be split into three peaks at 532.5, 535.5, and 537.7 eV (Fig. 1e). The first deconvoluted peak at 532.5 eV corresponds to the aliphatic C—O bond and the second peak at 535.5 eV belongs to the oxygen components adsorbed on the surface [34,35]. Oxygen atoms bonded to residual metals give rise to the peak at 537.7 eV [36].

Fig. 2**a,b** shows the scanning electron microscope (SEM) images at 50 and 10 μm magnifications. The ball-milled 6H graphite powder has particles made up of both flaky and spherical particle morphologies, with particle sizes ranging from nano to micrometers. The tunnelling electron microscope (TEM) images reveal the flake-like morphology of graphite (Fig. 2c). The TEM-assisted energy-dispersive X-ray spectroscopy (EDX) indicates the presence of C, O, Si, and N. The presence of nitrogen is not evident in XPS because of the limited surface penetration compared to the EDX technique.

The electrochemical performance of 6H pencil graphite was assessed in a half-cell with sodium metal foil as the counter and reference electrode with TEGDME and DEGDME-based electrolytes (labelled as 6H-G4 and 6H-G2). The electrochemical impedance spectroscopy was performed from 10 kHz to 1 Hz, with a voltage amplitude of 10 mV. From the impedance curve (Fig. 3a, 3b), the solution resistance is seen to be marginally higher for 6H-G2 (12.82 Ω) than 6H-G4 (12.04 Ω). Similarly, 6H-G4 has a lower charge transfer resistance (R_{CT}) of 43.74 Ω, while 6H-G2 shows an R_{CT} value of 59.47 Ω. Cyclic voltammetry (CV) curves of the half-cells were performed from 0.005 to 2.50 V *vs.* Na at a scan rate of 0.1, 0.2, 0.4, 0.6, 0.8, and 1.0 mV s^{-1} (Fig. 3b, 3d). The CV curves differ significantly in the anodic scan. In the CV of 6H-G4, at a scan rate of 0.1 mV s^{-1}, there is one prominent sharp peak at 0.48 V *vs.* Na, two small peaks at 0.08 and 0.38 V *vs.* Na, and a broad peak at 1.17 V *vs.* Na. However, the peak positions at 0.38 and 1.17 V *vs.* Na become much more pronounced at higher scan rates. The broad

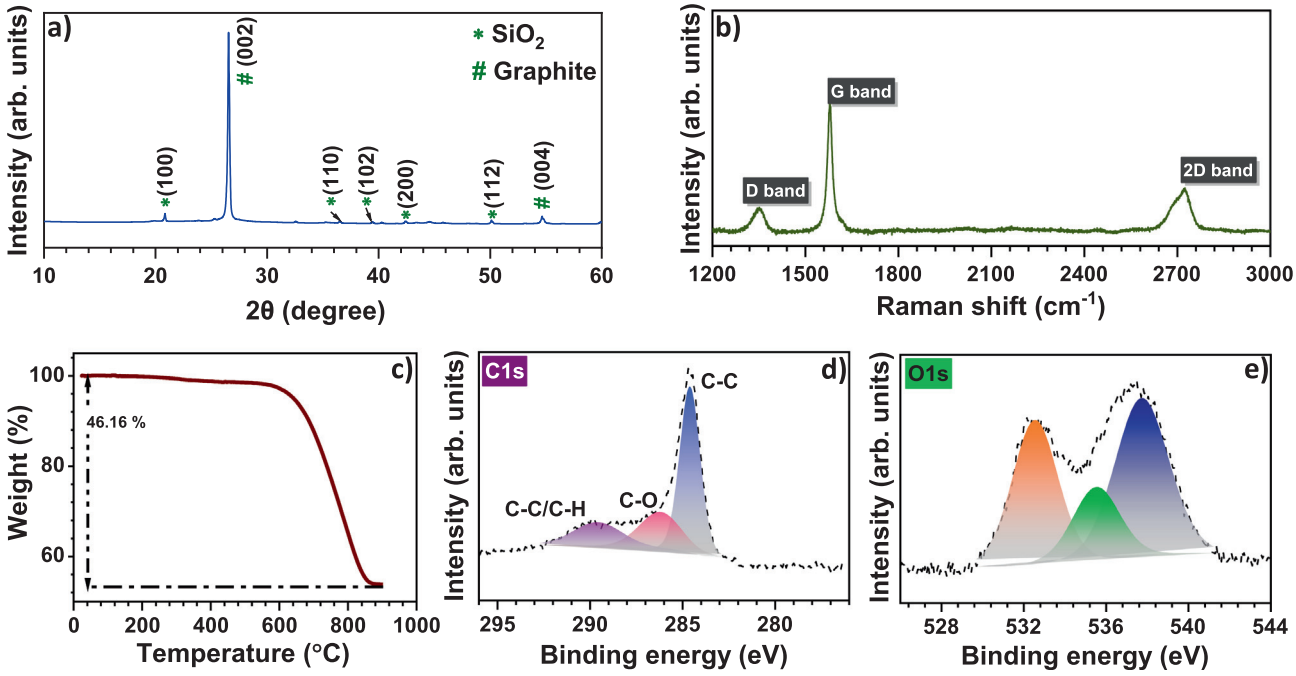

Fig. 1. (a) Powder XRD, (b) Raman spectra with D, G, and 2D bands, (c) TGA analysis, XPS spectra for (d) C1s, and (e) O1s of 6H pencil graphite.

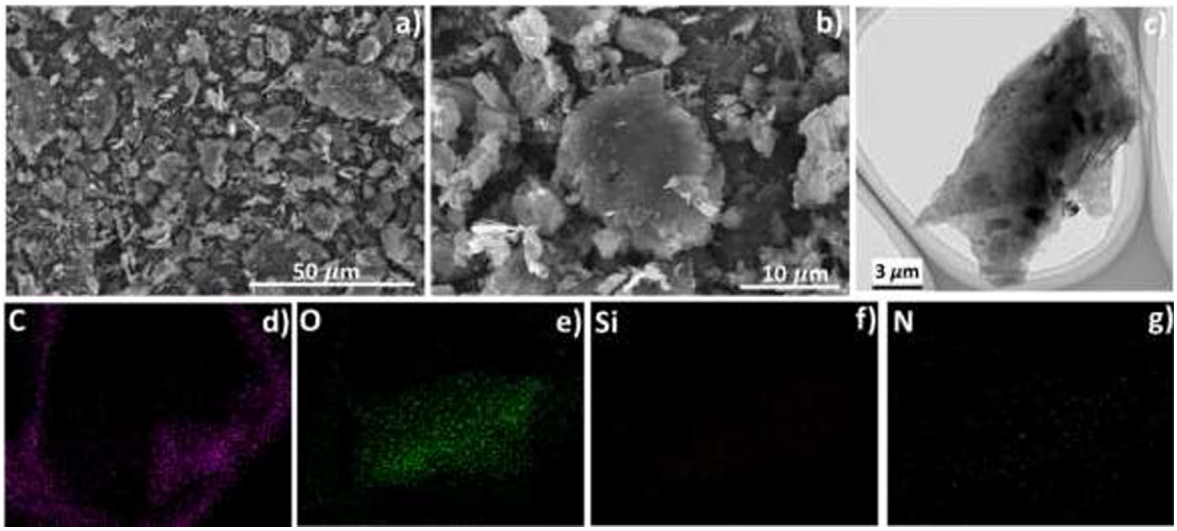

Fig. 2. (a,b) FE-SEM, (c) high-resolution TEM, and HR-TEM assisted elemental mapping of (d) C, (e) O, (f) Si, and (g) N.

peak at 1.17 V *vs.* Na indicates capacitive energy storage in 6H-pencil graphite. As for 6H-G2, there are small sharp peaks at 0.07, 0.15, and 1.64 V *vs.* Na, and a broad peak centered at 0.98 V *vs.* Na at a scan rate of 0.1 mV s^{-1}. The current values at 1.64 and 0.98 V *vs.* Na become higher with the scan rate. The broad peak in 6H-G2 has a higher current than 6H-G4, indicating higher capacitive energy storage in DEGDME. There are multiple peaks for both 6H-G4 and 6H-G2 during the reverse scan. At a scan rate of 0.1 mV s^{-1}, 6H-G4 shows multiple peaks at 0.01, 0.46, 0.72, 0.83, 0.93, and 1.13 V *vs.* Na, while 6H-G2 has cathodic peaks at 0.01, 0.14, 0.61, 0.71, 0.83, and 1.01 V *vs.* Na. 6H-G4 has a major peak at 0.72 V *vs.* Na, while 6H-G2 has a major peak at 0.61 V *vs.* Na. The peak potential deviation is proportional to the ethers' molecular chain length. As the scan rate increases, the voltage of the current peaks shifts, with the anodic scan shifting to a higher voltage and the cathodic scan shifting to a lower voltage. This behaviour is common in a diffusion-controlled process due to sluggish kinetics. The capacity contribution from the broad peak increases as the scan rate increases, indicating an increase in capacitive charge storage.

The absence of sharp peaks in the anodic scan of 6H-G2 CV is reflected in the galvanostatic charge–discharge (GCD) curves of 6H-G2 discharge, where the curves have more sloping regions than plateaus (Fig. 4f, 4 g). The 6H-G4 discharge curve has a plateau at 0.46 V *vs*. Na, which corresponds to a Faradaic reaction (Fig. 4b, 4c). Furthermore, at lower current rates, this plateau is more pronounced (Fig. 4c). Additionally, it is seen that the average working voltage of 6H-G4 is higher than 6H-G2, improving the half-cell's specific energy density. The average insertion potential for sodium in graphite using G4 as an electrolyte solvent is elevated/higher than G2 [37]. 6H-G4 and 6H-G2 were subjected to current rates of 25 to 1000 mA g^{-1} in the voltage window of 0.005 – 2.50 V *vs.*

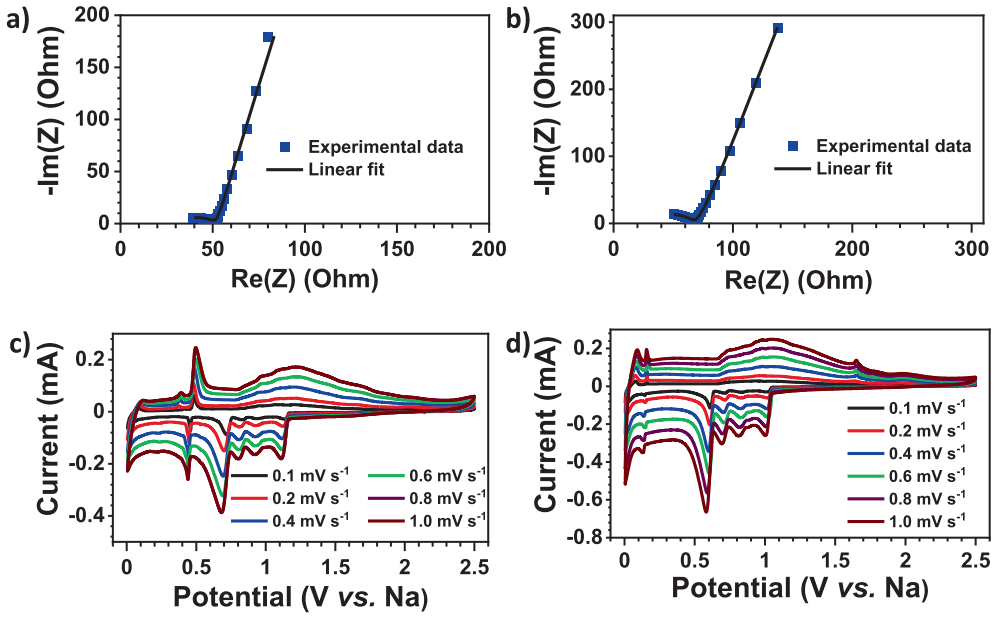

Fig. 3. Impedance data points with the linear fit for (a) 6H-G4, (b) 6H-G2, and CV curves at scan rates from 0.1 to 1.0 mV s^{-1} from 2.5 to 0.005 V *vs.* Na for (c) 6H-G4, (d) 6H-G2.

Na (Fig. 4a, 4e). The 6H-G2 displays better rate performance in terms of capacity at high current rates. The specific capacities of 113 and 66 mAh g^{-1} are observed at the current density of 1000 mA g^{-1} for 6H-G2 and 6H-G4, respectively. The G2-based cell has nearly twice the capacity of the G4-based system at high current. When returning to the initial current density after the high current, 6H-G4 exhibits little irreversibility and retains the initial capacity with little loss.

However, 6H-G2 has a poor Coulombic efficiency (CE) and shows a significant drop in discharge capacity. The long-term performance is recorded at a current density of 100 mA g^{-1} from 0.005 to 2.50 V *vs.* Na (Fig. 4d, 4h). 6H-G4 showed higher initial reversibility (43%), while 6H-G2 showed lower initial reversibility (39%). In the subsequent cycle, 6H-G4 had a discharge capacity of 171 mAh g^{-1}, while 6H-2G had 150 mAh g^{-1}. After 200 cycles, while 6H-G4 retained 82% of its initial discharge capacity, 6H-G2 maintained 87%. Regarding capacity at high current rates and long-term capacity retention, 6H-G2 outperforms 6H-G4. The 6H-G2 system, on the other hand, has significant Coulombic inefficiency (CI), which is especially noticeable when reverting to low current rates after applying a high current. Though 6H-G4 has CI, it is not as severe as 6H-G2. This inefficiency is caused by a side reaction occurring in the half-cell.

A more detailed investigation was performed on the 6H-G2 and 6H-G4 cells to understand the improved performance of 6H-G2 at high current rates. To begin with, a plot of the peak current against the square root of the scan rate of CV. This data was linearly fitted, whose slope is directly proportional to the diffusion coefficient according to the Randles-Sevcik equation, which is

$$i_p = 2.69 \times 10^5 n^{3/2} A C_0 D^{1/2} v^{1/2} \quad (1)$$

From the above equation,

$$D^{1/2} \alpha \frac{i_p}{V^{1/2}} \quad (2)$$

which is the slope of the i_p *vs.* v plot. Fig. 5**(a, b)** shows the slope for anodic and cathodic peak current linear fit for 6H-G4 and 6H-G2, respectively. 6H-G2 supports the Na-ion diffusion better because of the higher slope values in the G2 electrolyte system. This improved diffusion coefficient can be a factor for the superior rate performance of 6H-G2. Further, the capacitive and Faradaic-assisted charge storage mechanism was quantified using the current–voltage relation,

$$i = a v^b \quad (3)$$

Among the constants a and b, the value of b determines the charge storage mechanism. When b = 1, it represents a purely capacitive process, and b = 0.5 shows a pure battery-like behaviour. Then **Eqn. (3)** takes the form

$$i = a_1 v^{1/2} + a_2 v \quad (4)$$

Rearranging the above equation,

$$\log i = \log a + b \log v \quad (5)$$

When 0.5 < b < 1, the system has both mechanisms involved in charge storage. This value is determined for 6H-G4 and 6H-G2 from **Eqn. (5)**, where the latter shows a higher b value for anodic and cathodic scans, pointing to higher capacitive storage than the former. Capacitive mechanisms are more agile than Faradaic mechanisms, allowing for faster charge storage at higher current rates. Beyond this qualitative comparison, the quantitative estimation of the Faradaic and Capacitive charge storage was estimated using **Eqn. (4)** and plugging in the value of a, as shown in Fig. 5e. The capacitive charge storage mechanism contributes more than 50% of the capacity in 6H-G2 from the scan rate of 0.4 mV s^{-1} and beyond. In contrast, 6H-G4 has only 43% of the capacity contribution from capacitive storage even at a scan rate of 1 mV s^{-1}, and the dominant charge storage mechanism is Faradaic. The enhanced capacity at a high current rate of 6H-G2 is a synergy between an improved diffusion mechanism and the predominance of capacitive charge storage.

The 6H-pencil graphite was tested in a balanced full-cell assembly as an anode with TEGDME and DEGDME-based electrolytes and an NVPC cathode. 6H electrodes were pre-cycled five times prior to assembly. The supplementary information (SI) contains more information on pre-cycling and optimizing the mass of NVPC.

The morphological characterization of NVPC is done through SEM and HR-TEM (**Fig S2**). The elemental analysis and HAADF-

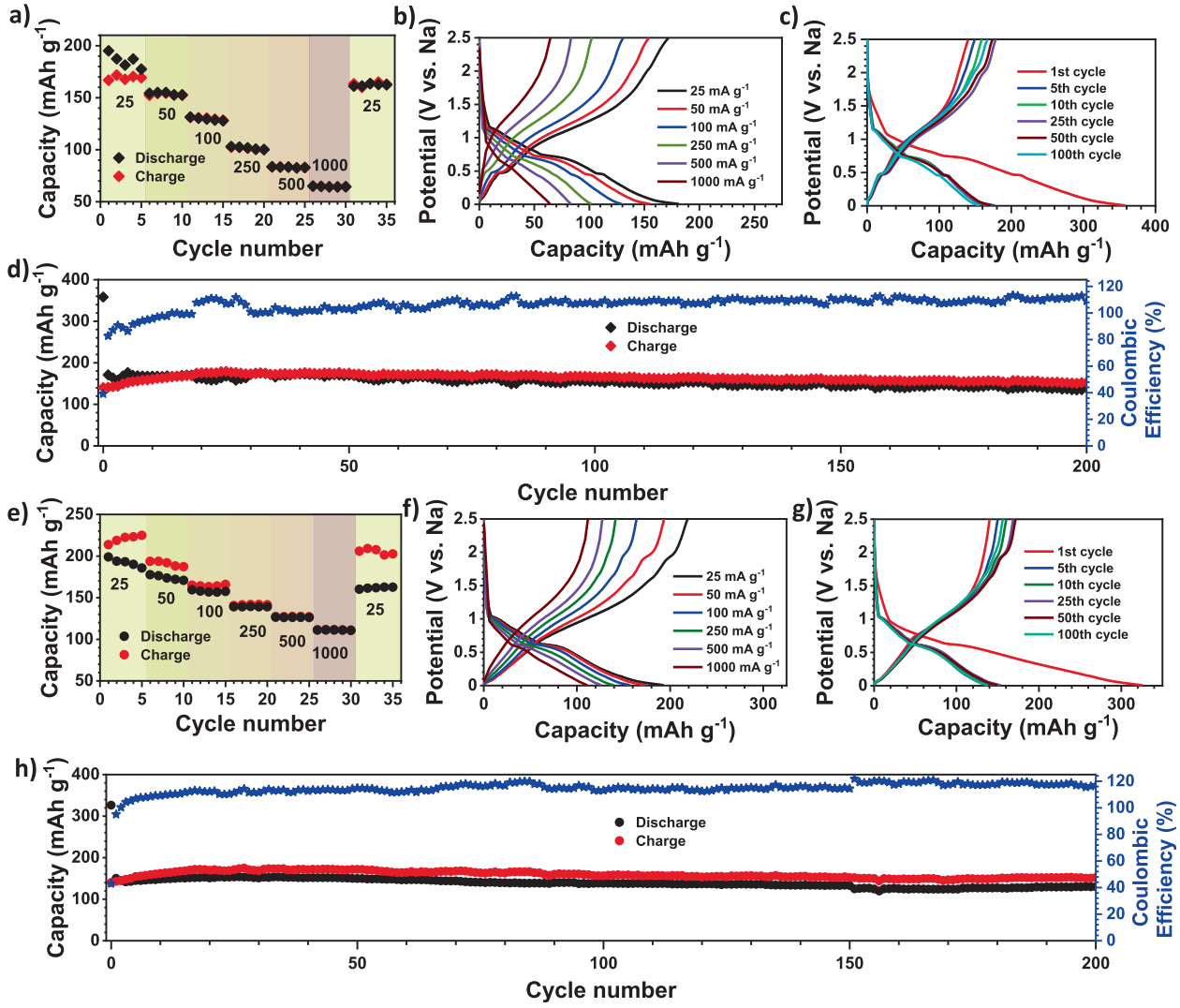

Fig. 4. Specific capacity at current rates of 25, 50, 100, 250, 500, and 1000 mA g^{-1} for (a) 6H-G4, (e) 6H-G2, GCD curves for the rate performance of (b) 6H-G4, (f) 6H-G2, GCD curves for cycles 1, 5, 10, 25, 50, and 100th cycles of (c) 6H-G4, and (g) 6H-G2, and long-term cycling test at a current density of 100 mA g^{-1} for (d) 6H-G4, (h) 6H-G2.

TEM of NVPC are shown in **Fig S3**. Further, the SI contains the XPS survey spectrum (**Fig S4**), XRD peak (**Fig S5a**), deconvoluted XPS peaks (**Fig S5b-f**), and Raman analysis (**Fig S5g**), and the TGA (**Fig S5h**) of NVPC. Electrochemical characterization of NVPC was performed with DEGDME and TEGDME-based electrolytes by assembling NVPC in a half-cell configuration. **Fig S6 and S7 show** the CV, rate performance, and long-term performance of the cells. Fig. 6a,e shows the Nyquist plot for full-cells. The applied frequency range and voltage amplitude are the same as that in half-cell studies. 6H-G4/NVPC has an R_{CT} value of 75 Ω, while 6H-G2/NVPC has an R_{CT} of ∼ 11.5 Ω. The former showed a prominent well-developed semi-circle in the Nyquist plot in the high-frequency region, while the latter showed a smaller semi-circle, similar to 6H-G2, but with a much lower R_{CT} value. This variation in R_{CT} suggests that the solid electrolyte interphase (SEI) layer characteristics of the full-cells differ. The CV of the full-cells recorded at a scan rate of 0.1 mV s^{-1} from 3.1 to 1.4 V is given in **Fig S8a, b**. The rate performance of the full-cells was studied at a current density of 25, 50, 100, 250, 500, 1000,1500, and 25 mA g^{-1} (Fig. 6**b, f**). The applied current density, in this case, is determined by the total mass loading of the active materials in both electrodes (NVPC and 6H). **Fig S8c, d** depicts the typical GCD curves for the rate performance**.** Like the half-cells, the DEGDME (Fig. 6b) based system exhibited the highest capacity at a current density of 1500 mA g^{-1}. However, capacity recovery after cycling at a high current was very poor in 6H-G2/NVPC. The cell exhibited a capacity of 27 mAh g^{-1} after five cycles at 25 mA g^{-1} initially. At the same time, cycling again at the same rate after the high current rate resulted in a loss of 56% of the earlier-mentioned capacity. 6H-G4/NVPC exhibited a better capacity than 6H-G2/NVPC at a current density of 25 mA g^{-1} (32 mAh g^{-1}) and maintained 90% of its capacity at a current density of 25 mA g^{-1} after switching back from high current testing. Clearly, the TEGDME-based full-cell shows dominance in the rate performance. Following that, the long-term performance of the full-cell was evaluated at a current density of 50 mA g^{-1} from 3.1 to 1.4 V. Despite the fact that the cell was assembled after pre-cycling, both cells demonstrated irreversibility in the first cycle, which was caused primarily by the cathode and freshly added electrolyte solution. The irreversibility was considerably higher in 6H-G2/NVPC, with a low initial CI of 41% (Fig. 6h), whereas the CI of 6H-G4/NVPC was 63.8 %. While the 6H-G2/NVPC system's CE is 87% after 100 cycles, the CE of the 6H-G4/NVPC system is 98% by the fourth cycle. The initial charge capacity of 6H-G2/NVPC is 172 mAh g^{-1} and retained a

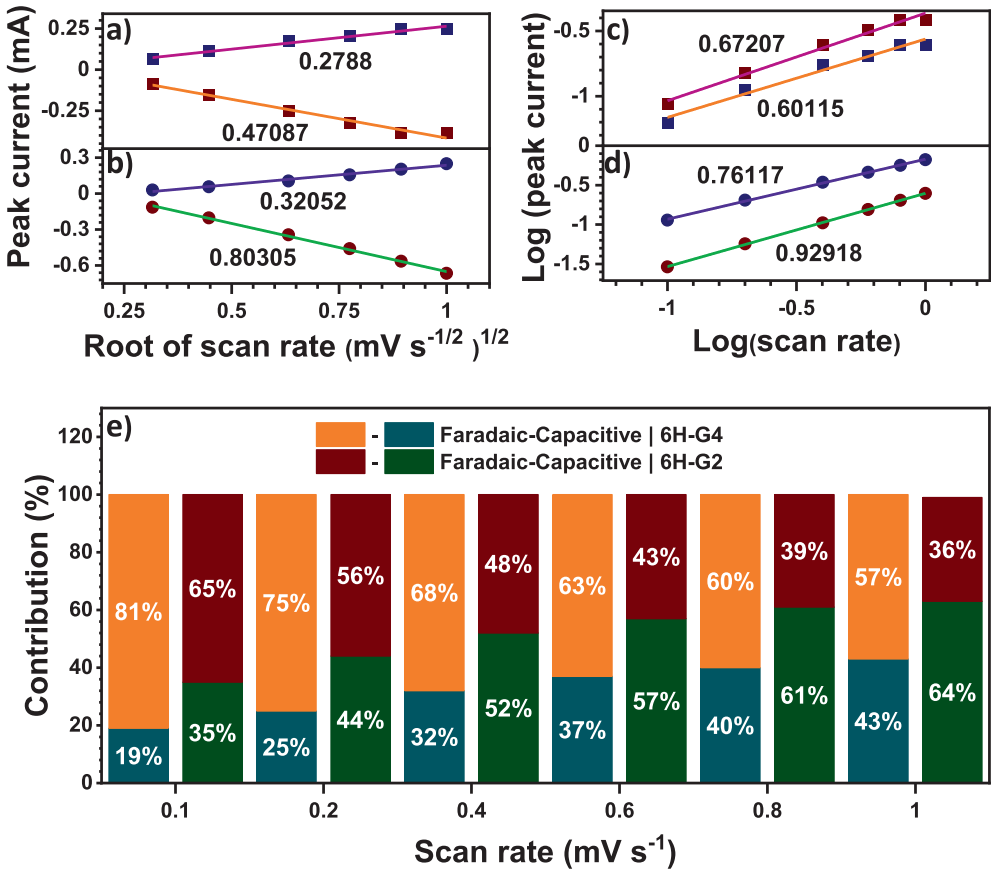

Fig. 5. Peak current *vs.* root of scan rate for (a) 6H-G4, (b) 6H-G2, log peak current *vs.* log scan rate for (c) 6H-G4, (d) 6H-G2, capacitive and Faradaic contributions for 6H-G4 and 6H-G2 solutions.

charge capacity of 74 mAh g^{-1} in the next cycle. Whereas 6H-G4/NVPC displayed an initial charge capacity of 105 mAh g^{-1} with a slight loss of charge capacity, resulting in 96 mAh g^{-1} in the second cycle. While the DEGDME-based full-cell displayed acute capacity degradation, the TEGDME-based full-cell had better retention capabilities. The former's discharge capacity is less than its corresponding charge capacity, which accounts for the low CE value. This degradation is associated with poor CE, resulting from the inevitable side reactions. The nature of the charge–discharge curve is similar in both the full-cells (Fig. 6**g,c**). As expected, the average operating voltage of 6H-G2/NVPC is higher than 6H-G4/NVPC, but this could not compensate for the capacity loss when calculating the energy density.

The full-cell performances were compared using a Ragone plot constructed with their specific energy and power densities, as shown in Fig. 7. The performance of 6H-G2/NVPC and 6H-G4/NVPC has been compared with recovered graphite/NVPC full-cell [38] in the Ragone plot. The calculations were performed based on the active material mass in the anode and cathode. Even with a higher operating potential, 6H-G2/NVPC had lower specific energy and power densities than 6H-G4/NVPC at all current rates tested. The maximum specific energy density of the TEGDME-full-cell was ~33 Wh kg^{-1} (~43 W kg^{-1}), and the maximum specific power density was ~2.7 kW kg^{-1} (~6.7 Wh kg^{-1}). At 25 mA g^{-1} and 1500 mA g^{-1}, the DEGDME-full-cell had a maximum energy density of ~23 Wh kg^{-1} (~26 W kg^{-1}) and a maximum specific power density of ~1.4 kW kg^{-1} (~3.6 Wh kg^{-1}). At all current rates, 6H-G4/NVPC performed significantly better than 6H-G2/NVPC. This apparent difference is due to the DEGDME system's poor stability, in which the CE has played the primary role.

4. Conclusion

We investigated the performance of 6H-pencil graphite as an anode for sodium-ion batteries in half and full-cell configurations by recycling pencil lead from commercially available pencils. Pencil graphite with the highest SiO_2 content (53.84%), confirmed by XRD, XPS, and quantified by TGA, was investigated as an anode in the sodium-ion battery where electrolytes with different solvents, namely TEGDME and DEGDME, were used. From half-cell and full-cell studies, it was observed that the specific capacity at high currents is better with G2-based electrolytes. Despite this, the cycling stability, capacity retention after subjecting to high current, and Coulombic efficiency of the full-cells are better with the G4 electrolyte, whereas 6H-G2 exhibited slightly better capacity retention. The capacity retention after 200 cycles at a current density of 100 mA g^{-1} was 87% for 6H-G2 and 82% for 6H-G4. At high current rates, 6H-G2 outperformed 6H-G4, with the former having twice the specific capacity of the latter at 1000 mA g^{-1}. However, the loss of capacity and irreversibility is prominent in 6H-G2 when reverted to the low current rate. The capacitive storage contribution was the dominant mechanism in 6H-G2, resulting in improved high rate performance. In contrast Faradaic reaction is the primary Na-ion storage mechanism in 6H-G4. At 1000 mA g^{-1}, 6H-G2 has a 63% capacitive mechanism-derived specific capacity, while 6H-G4 shows 57% Faradaic mechanism-derived specific capacity. The performance of 6H as an anode in a full-cell with an NVPC cathode was evaluated, and the TEGDME-based full-cell performed the best. 6H-G4/NVPC had a maximum specific energy density of 33 Wh kg^{-1}, and 6H-G2/NVPC had a maximum specific energy density of 23 Wh kg^{-1}, respectively. The performance of the full-cell has been

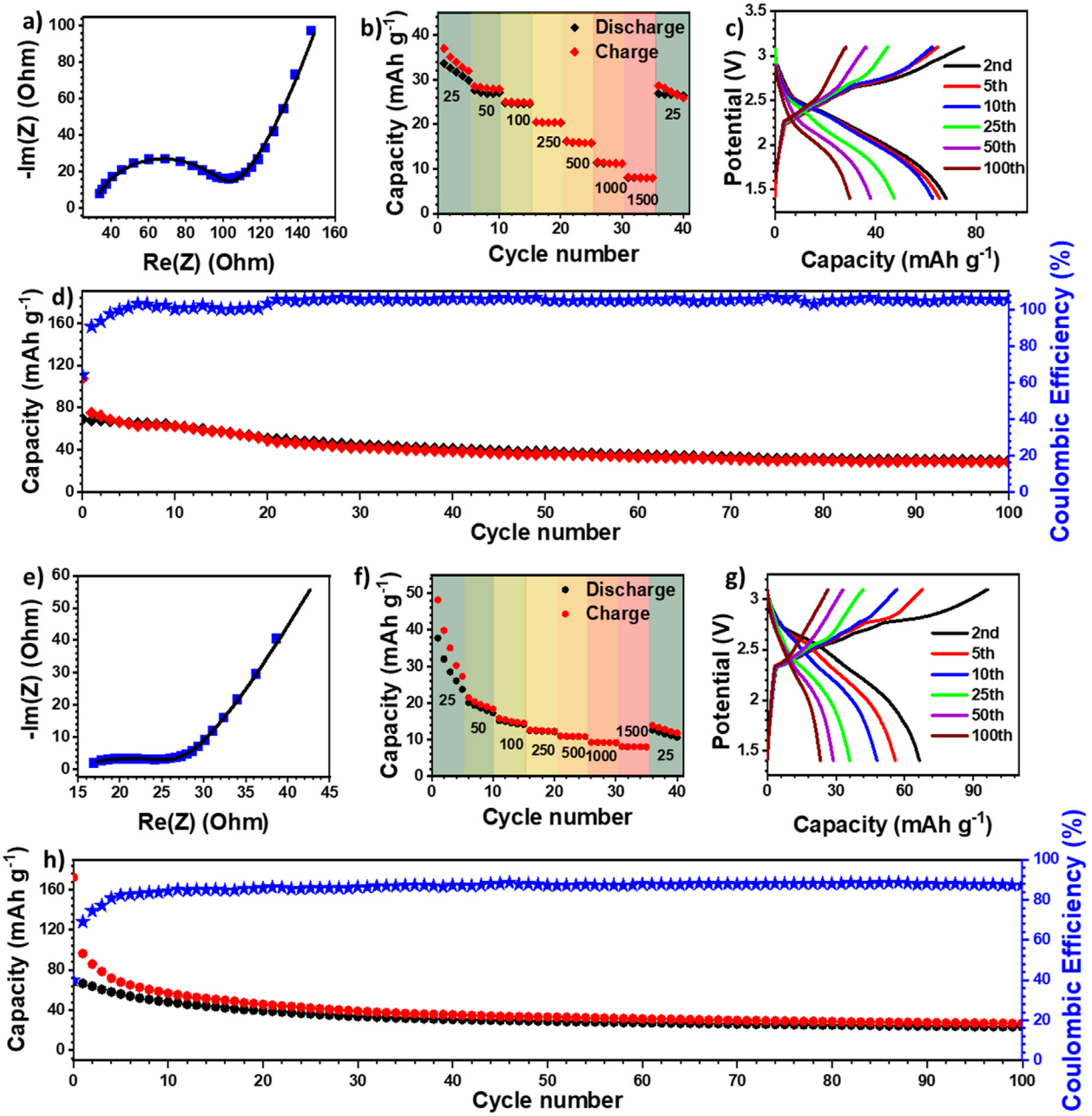

Fig. 6. Impedance data points with the linear fit for (a) 6H-G4/NVPC, (e) 6H-G2/NVPC full-cells, specific capacity at current rates of 25, 50, 100, 250, 500, 1000, and 1500 mA g^{-1} from 3.1 to 1.4 V for (b) 6H-G4/NVPC, (f) 6H-G2/NVPC full-cells, long-term cycling test at a current density of 50 mA g^{-1} for (d) 6H-G4/NVPC, (j) 6H-G2/NVPC from 3.1 to 1.4 V, and GCD curves for cycles 1, 5, 10, 25, 50, and 100th cycles of (f) 6H-G4/NVPC, and (l) 6H-G2/NVPC.

compared with RG/NVPC full-cell performance [38]. This is the first attempt at recovering and reusing pencil graphite with high-mass electrodes for sodium-ion battery application using ether-based electrolytes. Additional work should be performed to improve the Coulombic efficiency, drastically improving long-term cycling stability. Thermal treatment to ensure the optimal structure of graphite and electrolyte additives to improve the stability of electrolytes at high potential are some techniques to enhance the performance of 6H pencil graphite.

CRediT authorship contribution statement

Krishnan Subramanyan: Conceptualization, Methodology, Investigation, Data curation, Writing – original draft. **Yun-Sung Lee:** Project administration, Writing – review & editing, Supervision. **Vanchiappan Aravindan:** Conceptualization, Methodology, Investigation, Data curation, Writing – original draft, Project administration, Writing – review & editing, Supervision.

Data availability

Data will be made available on request.

Declaration of Competing Interest

The authors declare that they have no known competing financial interests or personal relationships that could have appeared to influence the work reported in this paper.

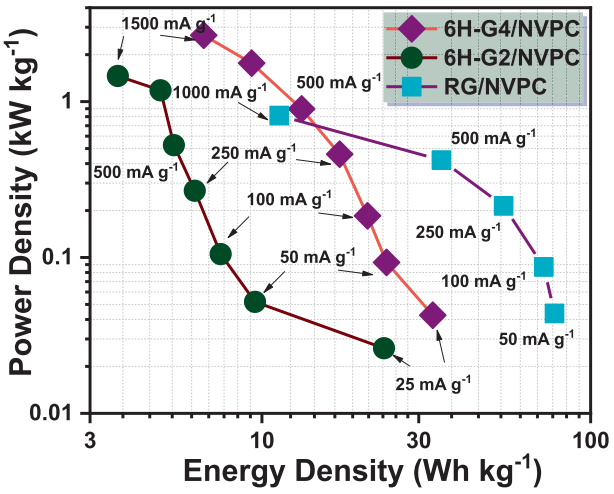

Fig. 7. Ragone plot for 6H-G4/NVPC and 6H-G2/NVPC compared with RG/NVPC [38].

Acknowledgements

KS thanks the Department of Science & Technology (DST), Govt. of India, for the financial support through INSPIRE fellowship (IF180157). YSL acknowledges the financial support from the National Research Foundation of Korea (NRF) grant funded by the Korean government (Ministry of Science, ICT & Future Planning) (No. 2019R1A2C1007620). VA acknowledges financial support from the Science and Engineering Research Board (SERB), a statutory body of DST, Govt. of India, through Swarnajayanti Fellowship (SB/SJF/2020-21/12)

Appendix A. Supplementary data

Supplementary data to this article can be found online at https://doi.org/10.1016/j.jcis.2022.11.053.

References

[1] J. Asenbauer, T. Eisenmann, M. Kuenzel, A. Kazzazi, Z. Chen, D. Bresser, The success story of graphite as a lithium-ion anode material-fundamentals, remaining challenges, and recent developments including silicon (oxide) composites, Sustain. Energy Fuels 4 (11) (2020) 5387–5416.
[2] Q. Chen, L. Huang, J. Liu, Y. Luo, Y. Chen, A new approach to regenerate high-performance graphite from spent lithium-ion batteries, Carbon N. Y. 189 (2022) 293–304.
[3] M. Valvo, C. Floraki, E. Paillard, K. Edström, D. Vernardou, Perspectives on Iron Oxide-Based Materials with Carbon as Anodes for Li- and K-Ion Batteries, Nanomaterials 12 (9) (2022) 1436.
[4] F. Duffner, N. Kronemeyer, J. Tübke, J. Leker, M. Winter, R. Schmuch, Post-lithium-ion battery cell production and its compatibility with lithium-ion cell production infrastructure, Nat. Energy 6 (2) (2021) 123–134.
[5] T. Placke, R. Kloepsch, S. Dühnen, M. Winter, Lithium ion, lithium metal, and alternative rechargeable battery technologies: the odyssey for high energy density, J. Solid State Electrochem. 21 (7) (2017) 1939–1964.
[6] K. Subramanyan, Y.-S. Lee, V. Aravindan, Impact of carbonate-based electrolytes on the electrochemical activity of carbon-coated $Na_3V_2(PO_4)_2F_3$ cathode in full-cell assembly with hard carbon anode, J. Colloid Interface Sci. 582 (2021) 51–59.
[7] K. Subramanyan, M.L. Divya, V. Aravindan, Dual-carbon Na-ion capacitors: progress and future prospects, J. Mater. Chem. A 9 (15) (2021) 9431–9450.
[8] H. Moriwake, A. Kuwabara, C.A.J. Fisher, Y. Ikuhara, Why is sodium-intercalated graphite unstable?, RSC Adv 7 (2017) 36550–36554.
[9] O. Lenchuk, P. Adelhelm, D. Mollenhauer, New insights into the origin of unstable sodium graphite intercalation compounds, Phys. Chem. Chem. Phys. 21 (35) (2019) 19378–19390.
[10] B. Jache, P. Adelhelm, Use of graphite as a highly reversible electrode with superior cycle life for sodium-ion batteries by making use of co-intercalation phenomena, Angew. Chem. Int. Ed. Engl. 53 (38) (2014) 10169–10173.
[11] Z.L. Xu, G. Yoon, K.Y. Park, H. Park, O. Tamwattana, S. Joo Kim, W.M. Seong, K. Kang, Tailoring sodium intercalation in graphite for high energy and power sodium ion batteries, Nat. Commun. 10 (2019) 1–10.
[12] G. Yoon, H. Kim, I. Park, K. Kang, Conditions for Reversible Na Intercalation in Graphite: Theoretical Studies on the Interplay Among Guest Ions, Solvent, and Graphite Host, Adv. Energy Mater. 7 (2) (2017) 1601519.
[13] H. Kim, J. Hong, G. Yoon, H. Kim, K.-Y. Park, M.-S. Park, W.-S. Yoon, K. Kang, Sodium intercalation chemistry in graphite, Energy Environ. Sci. 8 (10) (2015) 2963–2969.
[14] H. Kim, J. Hong, Y.-U. Park, J. Kim, I. Hwang, K. Kang, Sodium Storage Behavior in Natural Graphite using Ether-based Electrolyte Systems, Adv. Funct. Mater. 25 (4) (2015) 534–541.
[15] B. Yao, J. Zhang, T. Kou, Y.u. Song, T. Liu, Y. Li, Paper-Based Electrodes for Flexible Energy Storage Devices, Adv. Sci. 4 (7) (2017) 1700107.
[16] G. Zheng, L. Hu, H. Wu, X. Xie, Y. Cui, Paper supercapacitors by a solvent-free drawing method, Energy Environ. Sci. 4 (2011) 3368–3373.
[17] B. Yao, L. Yuan, X.u. Xiao, J. Zhang, Y. Qi, J. Zhou, J. Zhou, B. Hu, W. Chen, Paper-based solid-state supercapacitors with pencil-drawing graphite/polyaniline networks hybrid electrodes, Nano Energy 2 (6) (2013) 1071–1078.
[18] K. Chen, D. Xue, S. Komarneni, Nanoclay assisted electrochemical exfoliation of pencil core to high conductive graphene thin-film electrode, J. Colloid Interface Sci. 487 (2017) 156–161.
[19] A. Özcan, Y. Şahin, Preparation of selective and sensitive electrochemically treated pencil graphite electrodes for the determination of uric acid in urine and blood serum, Biosens. Bioelectron. 25 (11) (2010) 2497–2502.
[20] R. Navratil, A. Kotzianova, V. Halouzka, T. Opletal, I. Triskova, L. Trnkova, J. Hrbac, Polymer lead pencil graphite as electrode material: Voltammetric, XPS and Raman study, J. Electroanal. Chem. 783 (2016) 152–160.
[21] K. Aoki, T. Okamoto, H. Kaneko, K. Nozaki, A. Negishi, Applicability of graphite reinforcement carbon used as the lead of a mechanical pencil to voltammetric electrodes, J. Electroanal. Chem. Interfacial Electrochem. 263 (2) (1989) 323–331.
[22] R.L. McCreery, Advanced Carbon Electrode Materials for Molecular Electrochemistry, Chem. Rev. 108 (7) (2008) 2646–2687.
[23] J.K. Kariuki, An Electrochemical and Spectroscopic Characterization of Pencil Graphite Electrodes, J. Electrochem. Soc. 159 (9) (2012) H747–H751.
[24] L. Trnkova, I. Triskova, J. Cechal, Z. Farka, Polymer pencil leads as a porous nanocomposite graphite material for electrochemical applications: The impact of chemical and thermal treatments, Electrochem. commun. 126 (2021) 107018.
[25] Z. Tai, Y. Liu, Q. Zhang, T. Zhou, Z. Guo, H.K. Liu, S.X. Dou, Ultra-light and flexible pencil-trace anode for high performance potassium-ion and lithium-ion batteries, Green Energy Environ. 2 (3) (2017) 278–284.
[26] S. Mamidi, A.K. Pandey, A.D. Pathak, T.N. Rao, C.S. Sharma, Pencil lead powder as a cost-effective and high-performance graphite-silica composite anode for high performance lithium-ion batteries, J. Alloys Compd. 872 (2021) 159719.
[27] K.P. Shadiya, M.L. Divya, Y.-S. Lee, V. Aravindan, Pencil Scripted Ultrathin Graphene Nanostructure as Binder-Free Battery-Type Electrode for Li-Ion Micro-Capacitors with Excellent Performance, Energy Technol. 10 (2022) 2200205, https://doi.org/10.1002/ente.202200205. Available at:.
[28] M.L. Divya, Y.-S. Lee, V. Aravindan, Pencil Powered Faradaic Electrode for Lithium-Ion Capacitors with High Energy and Wide Temperature Operation, Batter. Supercaps 5 (2022) e202200214. Available at:.
[29] R. Klee, M.J. Aragón, R. Alcántara, J.L. Tirado, P. Lavela, High-Performance $Na_3V_2(PO_4)_3$/C Cathode for Sodium-Ion Batteries Prepared by a Ball-Milling-Assisted Method, Eur. J. Inorg. Chem. 2016 (19) (2016) 3212–3218.
[30] J.-B. Wu, M.-L. Lin, X. Cong, H.-N. Liu, P.-H. Tan, Raman spectroscopy of graphene-based materials and its applications in related devices, Chem. Soc. Rev. 47 (5) (2018) 1822–1873.
[31] L. Xiaowei, R. Jean-Charles, Y.u. Suyuan, Effect of temperature on graphite oxidation behavior, Nucl. Eng. Des. 227 (3) (2004) 273–280.
[32] R.I.R. Blyth, H. Buqa, F.P. Netzer, M.G. Ramsey, J.O. Besenhard, P. Golob, M. Winter, XPS studies of graphite electrode materials for lithium ion batteries, Appl. Surf. Sci. 167 (1-2) (2000) 99–106.
[33] G. Greczynski, L. Hultman, The same chemical state of carbon gives rise to two peaks in X-ray photoelectron spectroscopy, Sci. Rep. 11 (2021) 11195.
[34] M. Smith, L. Scudiero, J. Espinal, J.-S. McEwen, M. Garcia-Perez, Improving the deconvolution and interpretation of XPS spectra from chars by ab initio calculations, Carbon N. Y. 110 (2016) 155–171.
[35] S.O. Ganiyu, M.J.G. de Araújo, E.C.T. de Araújo Costa, J.E.L. Santos, E.V. dos Santos, C.A. Martínez-Huitle, S.B.C. Pergher, Design of highly efficient porous carbon foam cathode for electro-Fenton degradation of antimicrobial sulfanilamide, Appl. Catal. B Environ. 283 (2021) 119652.
[36] F.A. Chowdhury, M.A. Hossain, K. Uchida, T. Tamura, K. Sugawa, T. Mochida, J. Otsuki, T. Mohiuddin, M.A. Boby, M.S. Alam, Graphene oxide/carbon nanoparticle thin film based IR detector: Surface properties and device characterization, AIP Adv. 5 (10) (2015) 107228.
[37] Z.-L. Xu, G. Yoon, K.-Y. Park, H. Park, O. Tamwattana, S. Joo Kim, W.M. Seong, K. Kang, Tailoring sodium intercalation in graphite for high energy and power sodium ion batteries, Nat. Commun. 10 (2019) 2598.
[38] K. Subramanyan, M. Akshay, Y.S. Lee, V. Aravindan, Na-Ion Battery with Graphite Anode and $Na_3V_2(PO_4)_3$ Cathode via Solvent-Co-Intercalation Process, Adv. Mater. Technol. 2 (2022) 1–7.